



pubs.acs.org/journal/ascecg Research Article

Toward a Stackable CO₂-to-CO Electrolyzer Cell Design—Impact of Media Flow Optimization

Maximilian Quentmeier,* Bernhard Schmid, Hermann Tempel, Hans Kungl, and Rüdiger-A. Eichel



Cite This: ACS Sustainable Chem. Eng. 2023, 11, 679-688



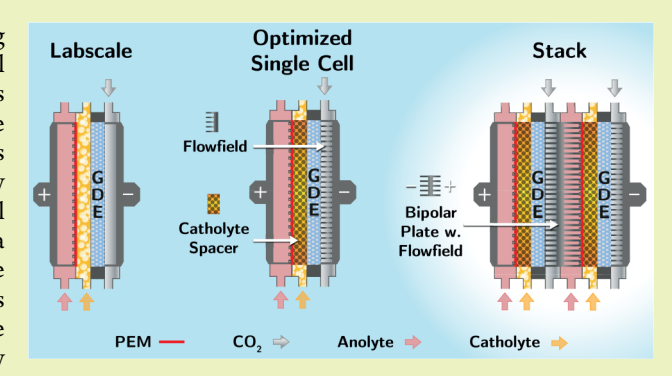
ACCESS

III Metrics & More

Article Recommendations

Supporting Information

ABSTRACT: Aqueous CO₂-to-CO electrolysis is a promising technology for closing the carbon cycle and defossilizing industrial processes. Considering the technological readiness, consensus has been achieved about using silver as a stable and selective electrocatalyst for the CO₂-to-CO reduction reaction in aqueous electrolyte. On the other hand, challenges such as media flow management, component stability, and force distribution are still associated with improving the process performance and developing a stackable cell concept to meet industrially relevant levels. We therefore report on a promising stack concept with continuous flowcells operated with gas diffusion electrodes (GDEs). To enhance the CO₂-to-CO conversion efficiency, dedicated media flow chambers were developed on two levels. In the gas chamber,



which touches the GDE from the far side of the anode, the feed gas flow and distribution over the GDE were controlled by introducing various gas path architectures in a modular flowcell. In addition, an ionically conductive spacer was implemented in the catholyte chamber, which is adjacent to the opposite side of the GDE. The effect of these modifications on the cell voltage, selectivity, and overall conversion was investigated at 100 mA/cm² with varying CO₂ feed gas flow and concentration. Noteworthy, an optimized feed gas distribution generated an increase of the Faraday efficiency for CO under reduced CO₂ supply. Furthermore, the implementation of the spacer enhanced the process stability by suppressing gas-bubble-induced noise in the cell voltage measurements. By functioning as support structures to the GDE, the combined modifications provided the cell with mechanical integrity and allowed an ionic and electric contact over the full active cell area, which is required for both stacking and upscaling of the cell. The corresponding performance was demonstrated by a two-cell short-stack.

KEYWORDS: carbon dioxide electroreduction, carbon monoxide, energy conversion, gas diffusion electrode, aqueous electrolytes

INTRODUCTION

The utilization of CO₂ as a feedstock for industrial processes can be a solution for closing carbon cycles and storing energy from renewable sources. A possible approach is the electrochemical reduction of CO₂ to platform chemicals. Despite significant interest in this process, the current state-of-the-art CO₂ electrolysis systems require improvements in energy efficiency and space time yield to enable the large scale production of CO₂ reduction products. Among different CO₂ reduction processes, the CO₂-to-CO electrolysis is one of the closest to meet technically and economically sensible production rates. While Ag is well established as a stable and selective electrocatalyst, the multitude of possible cell designs for the CO₂-to-CO electrolysis, that can be found in literature, reflects the difficulty of developing a mature process around the CO₂ reduction reaction.

Promising potential has been widely demonstrated with continuously operating mainly labscale flowcells, mostly working with aqueous media as electrolytes, which are separated by an ion exchange membrane. In this field gas

diffusion electrodes (GDEs) have widely replaced solid cathodes as they circumvent transport limitation stemming from the low solubility and slow diffusion of CO₂ in the electrolyte. Noteworthy, the choice of polymer electrolyte membrane has a major impact on the process and the design requirements for the cell. For instance, the use of proton exchange membranes has been shown to require an electrolyte buffer layer between the membrane and the GDE to reach good selectivity. The application of anion exchange membranes, on the other hand, enables use of a membrane electrode assembly construction, where the GDE is directly mated to the membrane, eliminating most of the electrolyte conduction resistance. Highest performances were dem-

Received: September 15, 2022 Revised: November 25, 2022 Published: January 4, 2023





onstrated with flowcells containing an anion exchange membrane, but the transport of HCO_3^- resulting in a parasitic CO_2 shuttling to the anode side remains an issue. ¹³ With proton exchange membranes, on the other hand, the ion flux in the form of protons is from the anode to the cathode compartment, thus preventing this undesired crossover. ¹⁴

While these membranes have outstanding ionic conductivity, they require the aforementioned buffer layer between the GDE and the membrane (Figure 1), ideally with a high to neutral

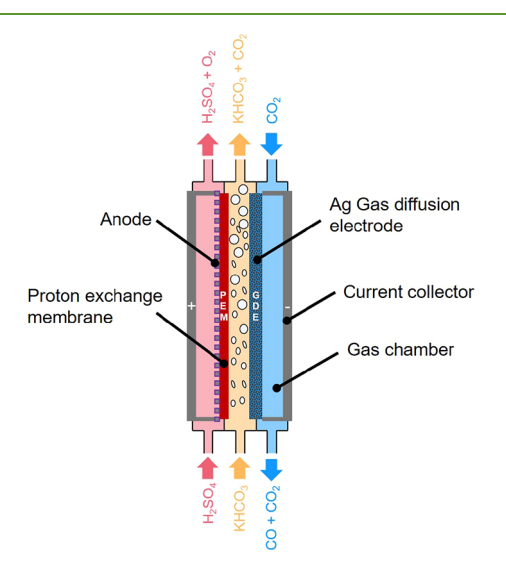


Figure 1. Illustration of a flowcell assembled with a zero-gap anode, proton exchange membrane and an Ag GDE, operating with H_2SO_4 as anolyte and KHCO₃ as catholyte.

pH value to suppress the hydrogen evolution reaction (HER) at the cathode's surface. 1,4,13 In many cases a KHCO $_3$ solution is used as the buffer layer, causing the protons to react at the membranes surface with HCO $_3^-$ to CO $_2$ and H $_2$ O. 4,6,15 Inevitably bubbles are formed in the catholyte, creating voids in the current flow, resulting in a higher and unstable cell voltage. 15 On the other hand the formation of CO $_2$ in the electrolyte offers the opportunity to recover CO $_2$, which can be introduced to the feed gas.

Even though the CO_2 recovery supports the reduction of CO_2 usage in the process, the CO_2 consumption remains an issue in the CO_2 -to-CO electrolysis.^{6,16} The exergonic HCO_3^- formation by the reaction of CO_2 with OH^- , favored in alkaline environments, increases the cell voltage and forces the state of the art CO_2 -to-CO electrolyzers to operate with CO_2 in excess to sufficiently suppress the $HER.^{13,16}$ As recent studies show, the management of the feed gas delivery to the GDE impacts the conversion rates of CO_2 . The formation of concentration gradients in a meander gas path along the GDE for instance enables only a partial exploitation of the GDE for the CO_2 -to-CO conversion.¹⁷

Regarding the anode side of the CO₂ electrolyzer, it is feasible to adopt the anode from the polymer electrolyte membrane water electrolysis (PEM).² For this study an even simpler and more robust zero-gap anode design is used. The proton exchange membrane enables the use of an acid as anolyte, which conditions a steady state operation of the electrolyzer.¹⁸ The protons, which are delivered to the cathode, are provided by the acid and reproduced at the anode. It should be noted, that while PEM-electrolyzers typically operate

with pure water, the use of a PEM-anode in CO₂-reduction still requires an acid in the electrolyte to compensate for the osmotic pressure from the catholyte buffer.

Furthermore, the adoption of the PEM-anode leads to the major advantage of harnessing an already existing and mature component, which is specifically of interest for the scale up of the system.² As the CO₂ electrolysis is a rather young technology, the scaling of CO2 electrolyzers operating at ambient conditions is barely discussed in the literature. 9,14,19,20 In electrolysis processes the scale ups are, aside from increasing the cell size, commonly performed by the stack assembly of multiple cells, which requires mechanically stable cell components. 19,21,22 These components function as supporting structures to the GDE and enable an even force distribution, while simultaneously managing the media flow distribution within the cell. The bipolar plate, which connects the cells in the stack and serves as a carrier of two poles plays a decisive role in this respect.^{23,24} Furthermore, the components define the management of the media manifolding, thus drawing attention to the periphery of the experimental setup as well as to shunt currents and equal media flow distribution within the stack. 24,25

The aim of this study is to optimize the performance of a single flowcell under the condition of creating a stackable flowcell architecture. By implementing flowfields with various gas path architectures in the gas flow compartment and in the form of a spacer in the catholyte flow compartment, this work addresses the effect of the optimization of the feed gas delivery and distribution over the GDE area on the flowcells performance, as well as the optimization of the catholyte flow compartment. The cell design utilized in this work is presented in Figure 1 and is based on a flowcell which was reported to be operating for over 1000 h with a cell voltage of about $-4.1 \, \text{V}$ at a current density of $100 \, \text{mA/cm}^2.6$

METHODS AND MATERIALS

The investigated cell (Figure 1) was assembled with the Micro Flow Cell from ElectroCell (Europe, Denmark), containing two electrolyte chambers with a depth of 2 mm and providing an active electrochemical area of 10 cm². The electrolyte chambers were separated by a Nafion 212 membrane (Sigma-Aldrich). The flowcell was assembled with the cathode electrode for carbon dioxide electrolyzer from Dioxide Materials. 12 A titanium mesh with an Ir-MMO coating and a mesh width of 4 mm × 2 mm was purchased from Metakem and used as a zero-gap anode. The anode and the GDE were 4 mm apart. H₂SO₄ (Honeywell Fluka) and KHCO₃ (Honeywell Fluka) were prepared with ultrapure water (PURELAB flex) to a 1 M H2SO4 and a 1 MKHCO3 solution and used as anolyte and catholyte. The electrolytes were circulated with a volume flow of 50 mL/min through the cell from reservoirs containing 250 mL of the electrolytes. After passing the cell, the gas appearing in the catholyte was separated from the catholyte with a membrane contactor (3M Liqui-Cel). The product gas from the cathode and the separated gas from the catholyte were analyzed separately via a Trace 1310 Thermo Scientific gas chromatograph and quantified via a drum style gas counter or a MilliGas counter (for gas flows below 20 mL/min). A total quantification for one gas stream took 12 min, thus generating a full data point containing both gas flows took 24 min. Three full data points were averaged to one measurement. All experiments were performed with a PGSTAT302N potentiostat (Metrohm), operating in galvanostatic mode at 1 A (100 mA/cm²). Further information on the used materials and devices can be found in the Supporting

Experiments were conducted under different CO_2 supply rates and were connected to the experimental parameter λ , which has been introduced in literature to describe the CO_2 excess in the experiment.⁶

 λ is defined as the ratio of the volumetric amount of $\mathrm{CO_2}(\dot{V}_{\mathrm{CO_2}})$ supplied to the cell, to the theoretical maximal producible volumetric amount of CO ($\dot{V}_{\mathrm{CO_{max}}}$) (eq 1). The maximum volumetric formation rate of CO can be calculated with the Faraday constant F, the amount of transferred electrons z, the molar volume of CO ($V_{\mathrm{CO_{mol}}} = 24.4 \, \mathrm{L/mol}$), and the total cell current I_{Cell} (eq 2). According to literature a $\lambda \geq 3$ is necessary to sufficiently suppress the HER in $\mathrm{CO_2}$ electrolyzers operating with neutral to alkaline catholyte buffers.

$$\lambda = \frac{\dot{V}_{\rm CO_2}}{\dot{V}_{\rm CO_{max}}} \tag{1}$$

$$\dot{V}_{\rm CO_{max}} = \frac{V_{\rm CO_{mol}}}{zF} I_{\rm Cell} \tag{2}$$

 λ was varied by two different methods: (1) varying the partial pressure of $\mathrm{CO}_2(p_{\mathrm{CO}_2})$ in the feed gas by the substitution of argon, while maintaining a constant feed gas volume flow at 35 mL/min; (2) operating with pure CO_2 gas and varying the feed gas volume flow.

The experiments with diluted CO_2 feed gas are reminiscent of the direct CO_2 -to-CO conversion in flue gas and it can portray the cell's behavior toward the cell's exit, where the feed gas is diluted due to the formation of products. Experiments with pure CO_2 gas were performed to increase the product concentrations in the product gas and to detect possible mass transport limitations at low feed gas volume flows. For all experiments one measurement point was generated for the λ -values 4.5, 3, 2, and 1, while λ = 4.5 was the starting value and λ was subsequently reduced. In experiments with a pure CO_2 supply, λ was additionally reduced to 0.5.

The experiments were conducted with cells containing various structures in the gas chamber or flowfields (titanium grade 1) with different gas path architectures. The flowfields and structures were characterized by the obtained Faraday efficiency for CO (FE(CO)), the cell voltage (U_{Cell}) and the determined concentrations of CO (φ_{CO}) and CO₂(φ_{CO_2}) in the product gas from the cathode. FE(CO) was calculated with the molar flow of CO (\dot{n}_{CO}) measured in the product gases from the cathode and the catholyte (eq 3).

$$FE(CO) \% = \frac{z\dot{n}_{CO}F}{I_{Cell}}100$$
(3)

 $U_{\rm Cell}$ was measured between the anode and the cathode. $\varphi_{\rm CO}$ and $\varphi_{\rm CO_2}$ were calculated via the volume flow of CO/CO₂ ($\dot{V}_{\rm CO_{out}}/\dot{V}_{\rm CO2_{out}}$) based on the data obtained by the gas chromatograph and the total volume flow of the product gas ($\dot{V}_{\rm tot_{out}}$) determined by the gas counters (eq 4).

$$\varphi_{\text{CO/CO}_2} \% = \frac{\dot{V}_{\text{CO}_{\text{out}}/\text{CO}_{\text{2out}}}}{\dot{V}_{\text{tot}_{\text{out}}}} 100 \tag{4}$$

RESULTS AND DISCUSSION

In order to design a stackable flowcell, flowfields providing a supporting structure to the GDE and managing the feed gas distribution were implemented at the gas side of the flowcell. In experiments, two flowfields with different gas path architectures were investigated, and their influence was compared to the cell's performance with an open frame current collector (Chamber1) (Figure 2(a)). One flowfield provided a meander gas path (Meander), the other one (Rake1) contained a disconnected gas path with several interlocking branches (Figure 2(a)). The open frame current collector contacts the GDE via the GDE's edges and provides thereby a gas chamber over the full active GDE area with a volume of 4 mL. The maximized GDE-gas contact area given by Chamber1 enables the feed gas to have a minimal diffusion

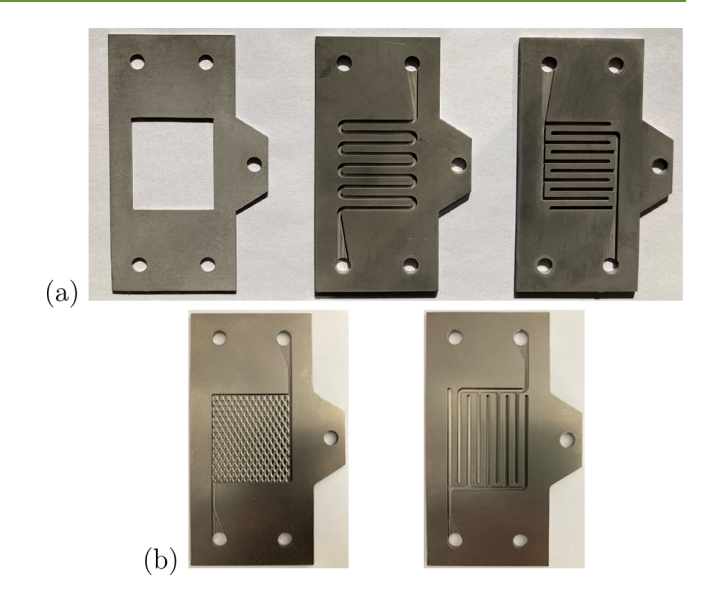


Figure 2. (a) Images of the first generation of the current collector providing a gas chamber (Chamber1, (a)-left), the flowfield with a meander gas path (Meander, middle), and the flowfield with interlocking gas path branches (Rake1, (a)-right). (b) Images of the second generation of the open frame current collector providing a gas chamber with an implemented titanium mesh (Chamber2, (b)-left) and the second generation of the rake flowfield providing the interlocking branches in a vertical orientation (Rake2, (b)-right).

length to the entire electrocatalyst area and can thus increase the conversion of CO₂-to-CO. But it also implies the reduction of the GDE-current collector contact area to a minimum, causing the GDEs' electric in-plane resistance to influence U_{Cell} to a greater extent. The flowfields provide, with 45% (Meander) and 50% (Rake1) of the active GDE area, larger GDE-current collector contact areas and can consequently reduce the impact of the GDEs' electric resistance on U_{Cell} . For Meander, the GDE-gas contact area can be determined to be 55% of the GDE's active area and is thus considerably lower than with Chamber1. The reduction of the GDE-gas contact area could diminish the CO2-to-CO conversion by hindering the transport of CO₂ to and the products from the electrocatalyst layer. Evaluating the GDE-gas contact area for Rake1 is less straightforward. The disconnected gas path forces the feed gas through the back side of the GDE and generates at best a GDE-gas contact area over the full active GDE area. Furthermore, the branches in Rake1 essentially segment the gas compartment, with each segment baring individual concentration gradients. Hence, Rake1 induces positive effects on FE(CO) and U_{Cell} simultaneously, by creating a more efficient trade-off between the GDE-gas contact and GDEcurrent collector contact area.

In addition, a second generation of the open frame current collector (Chamber2) and the rake flowfield (Rake2) (Figure 2(b)) were designed and tested based on the results obtained with the first generation. Chamber2 provides a gas chamber with a depth of 1 mm and a volume of 1 mL, in which a titanium expanded metal (1 mm thick) with a mesh width of 4 mm × 2 mm was inserted as a baffle. To reduce the cell voltage and to reduce the formation of concentration gradients possibly forming in Chamber1, Chamber2 provides a larger GDE-current collector contact area and a gas chamber with a smaller volume. Rake2 was designed similar to Rake1 but with a vertical orientation of the branches, to accelerate the removal

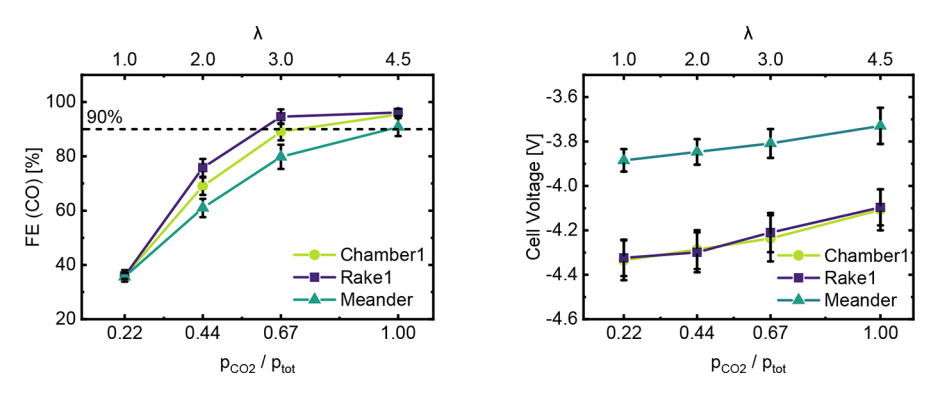


Figure 3. FE(CO) (left) and cell voltage (right) over different *λ*-values and p_{CO_2} in feed gas for experiments with Chamber1, Rake1, and Meander at 100 mA/cm².

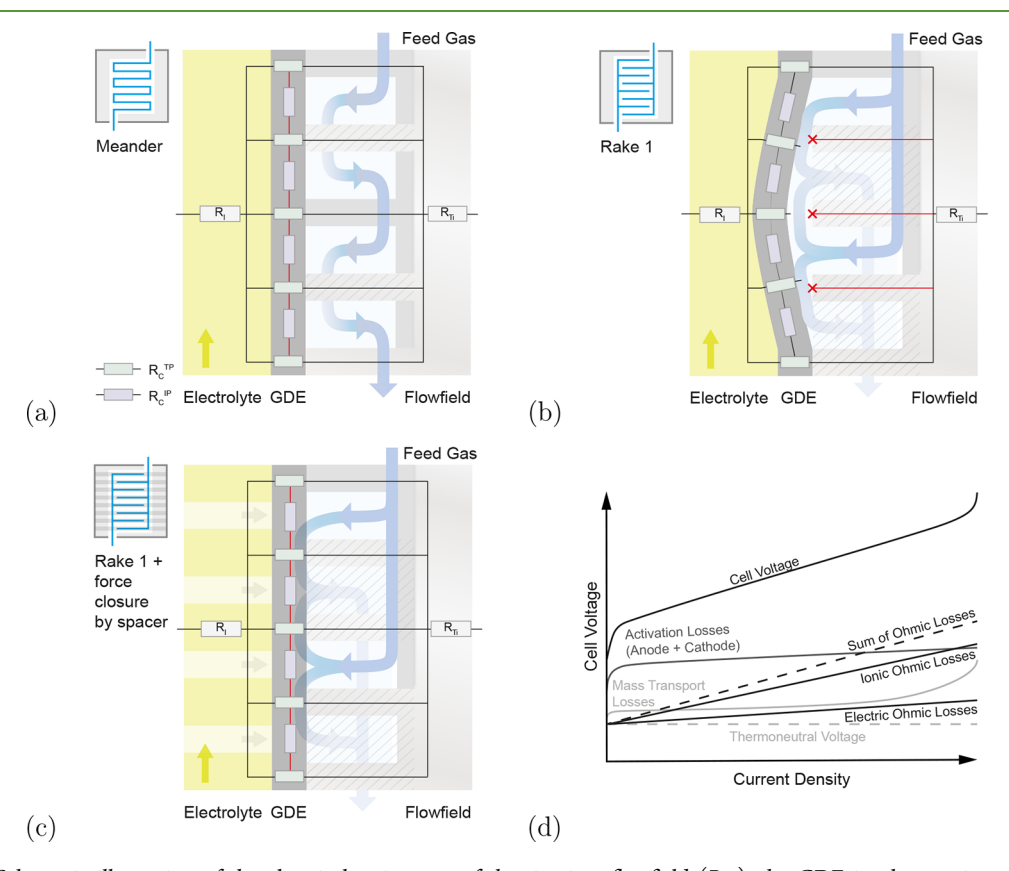


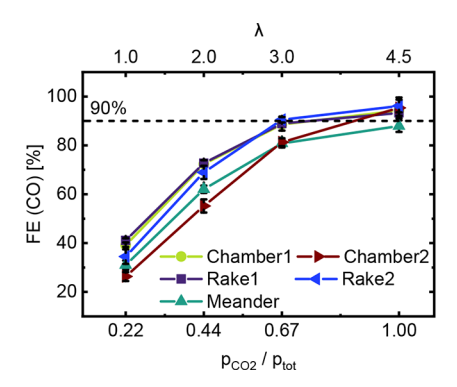
Figure 4. (a–c) Schematic illustration of the electrical resistances of the titanium flowfield ($R_{\rm TI}$), the GDE in plane resistance ($R_{\rm C}^{\rm IP}$), the ionic resistance of the electrolyte ($R_{\rm I}$) and the behavior of GDE on different flowfields. (a) GDE lies vertically on the meander, electrical current can pass along the flowfield. (b) Pressure generated by feed gas in Rake1 pushes GDE toward electrolyte and decreases GDE-current collector contact area, electrical current path is forced through in plane area of the GDE. (c) Force induced by a spacer pushes GDE onto Rake1, electrical current can pass along flowfield. (d) Influence of loss-mechanisms possibly affecting the cell voltage of electrolyzers over current density, expanded adaption from Endrődi et al.

of possible permeate in the gas chamber, which, if not removed from the gas chamber, reduces the cell performance by blocking the GDE-gas contact area. ²⁶

The results of the electrochemical experiments with the flowcell operating with diluted feed gas and containing Chamber1, Rake1, and Meander are depicted in Figure 3, showing the determined FE(CO) (left) and U_{Cell} (right) over λ and p_{CO_2} in the feed gas. In every experiment, a decreasing FE(CO) for decreasing λ -values can be observed. With Chamber1 and Rake1, FE(CO) maintained over 90% for $\lambda \geq 3$, with Meander FE(CO) $\geq 90\%$ determined for $\lambda = 4.5$. At $\lambda = 1$ FE(CO) decreased to a value of 35% in every

experiment. In all experiments, U_{Cell} increased with decreasing λ . Similar U_{Cell} was measured in experiments with Rake1 and Chamber1, increasing from $U_{\text{Cell}} = 4.1 \text{ V}$ at $\lambda = 4.5 \text{ to } U_{\text{Cell}} = 4.3 \text{ V}$ at $\lambda = 1$. Lower U_{Cell} can be observed for Meander decreasing from $U_{\text{Cell}} = 3.75 \text{ V}$ at $\lambda = 4.5 \text{ to } U_{\text{Cell}} = 3.9 \text{ V}$ at $\lambda = 1$.

The results in Figure 3 show a relation between the GDE-gas contact area and FE(CO) for diluted CO₂ supply. Rake1 and Chamber1 provide the largest GDE-gas contact area and show the highest FE(CO). A sufficient suppression of the HER (FE(CO) \geq 90%) could be maintained for Rake1 and Chamber1 for $\lambda \geq$ 3 ($p_{\rm CO_2} \geq$ 0.67). Further reduction of



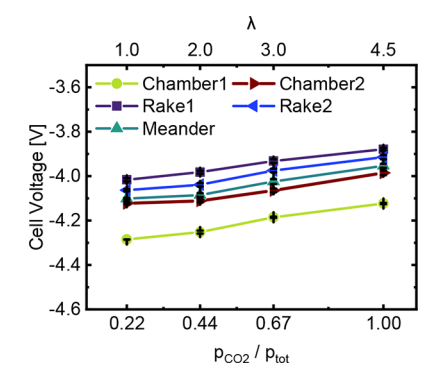


Figure 5. FE(CO) (left) and cell voltage (right) over different λ -values and p_{CO_2} in feed gas for experiments with Chamber1, Chamber2, Rake1, Rake2, and Meander in cell with spacer at 100 mA/cm².

 CO_2 supply led to an increase of the HER. Hence, higher U_{Cell} were determined with decreasing λ in every experiment. Minimal U_{Cell} were determined with Meander. As Meander provides a comparatively large GDE-current collector contact area, the electrical current, following the lowest electrical resistance, is led along the titanium flowfield rather than along the in-plane area of the GDE (Figure 4a). The electrical ohmic losses and thus the sum of the ohmic losses are reduced. The ohmic losses can be considered as a part of the loss mechanisms in an electrolyzer affecting the cell voltage (Figure 4d), hence a lower U_{Cell} is determined for Meander than for Chamber 1. With Rake 1 however, the determined U_{Cell} is similar to U_{Cell} determined for Chamber1 despite the larger GDE-current collector contact area provided by Rake1. As illustrated in Figure 4b, forcing the gas through the GDE with Rake1 increases the pressure on the gas side, the GDE is pushed toward the catholyte chamber, and the GDE-current collector contact area is reduced. This effect forces the electric current along the in-plane area of the GDE rather than along the titanium flowfield and increases thereby the electrical ohmic losses. To counteract the force originating from the pressure on the gas side of the cell, a spacer needs to be implemented inside the catholyte chamber. This spacer needs to complete the force closure within the cell to ensure full contact of the GDE to Rake1 (Figure 4c).

Spacers in electrolyte chambers can hinder the removal of gas bubbles by blocking their path toward the chamber's exit. This causes a reduction of the ionic conductivity through the electrolyte chamber, leading to an increase of cell voltage and a decrease of the overall cell performance.²⁷ To minimize this issue and to avoid isolating effects an ionically conductive hydrophilic spacer was implemented. Ion exchange resin (IER) beads were used to fill the catholyte chamber. The use of IERs in electrodionization processes or electrodialysis, to increase the conductivity in electrolyte chambers to reach cell voltage reduction, has already been shown in the literature.²⁸⁻³¹ Regarding CO₂ electrolysis, a hydrophilic and strongly acidic cation exchange resin was employed in CO2 to formic acid electrolysis.³² The IER was implemented as a flow through polymer electrolyte, to increase conductivity in the electrolyte chamber. In this work, the same IER was implemented as a spacer. Its effect on the electrolyte's conductivity was measured. A conductivity of 55 mS/cm was measured in a test tube with a 1 M KHCO₃ solution and the IER, for a pure 1 M KHCO₃ solution a conductivity of 73 mS/cm was determined. The exact procedure of the conductivity measurement is described in the Supporting Information.

The results obtained in the electrochemical experiments with the cell containing the spacer and operating with diluted feed gas are illustrated in Figure 5. For the first and the second series of flowfields, the determined FE(CO) and U_{Cell} are shown over λ and p_{CO_2} . In all experiments a decrease of FE(CO) with decreasing λ can be observed, starting at FE(CO) \geq 90% for λ = 4.5. With Rake1, Rake2, and Chamber1, FE(CO) remained over 90% until λ = 3 and decreased with further reduction of λ to 35% (Rake1, Chamber1) and 37% (Rake2) for λ = 1. A more rapid decrease of FE(CO) can be observed for Meander and Chamber2, with a determined FE(CO) = 80% for λ = 3 decreasing to 30% and 28% for λ = 1.

In every experiment, $U_{\rm Cell}$ increased with decreasing λ . With Rake1 and Rake2, $U_{\rm Cell}=3.88$ V and $U_{\rm Cell}=3.9$ V were determined for $\lambda=4.5$ increasing to $U_{\rm Cell}=4$ V and $U_{\rm Cell}=4.05$ V for $\lambda=1$. Higher cell voltages were determined with Meander and Chamber2 increasing from $U_{\rm Cell}=3.95$ V and $U_{\rm Cell}=4$ V for $\lambda=4.5$ to $U_{\rm Cell}=4.1$ V at $\lambda=1$. Similar to that in previous experiments, highest cell voltages were determined with Chamber1 increasing from $U_{\rm Cell}=4.1$ V at $\lambda=4.5$ to $U_{\rm Cell}=4.3$ V at $\lambda=1$.

The determined FE(CO) values for Chamber1, Rake1, and Meander show similar characteristics to the previous results without the spacer (Figure 3). In both cases, higher FE(CO) values were obtained when larger GDE-gas contact areas were provided. Rake2 provides a similar GDE-gas contact area to Rake1 and similar FE(CO) values were obtained. Despite the large GDE-gas contact area, given by Chamber2, a stronger decrease of FE(CO) can be observed compared to the other experiments. Due to the mesh structure in Chamber 2, a removal of accruing permeate is difficult, the accumulating permeate in the gas chamber blocks parts of the GDE-gas contact area and diminishes the conversion of CO₂-to-CO. However, the mesh structure increases the GDE-current collector contact area of Chamber2 compared to Chamber1 and reduces U_{Cell} . But the low FE(CO) indicates an increased appearance of the HER resulting in higher U_{Cell} for Chamber2 compared to the flowfields.

Comparing the $U_{\rm Cell}$ values for Rake1 obtained with (Figure 5) and without (Figure 3) the spacer, a significant decrease of $U_{\rm Cell}$ from 4.1 V to 3.88 V for λ = 4.5 can be observed with the spacer implementation. As illustrated in Figure 6, the spacer provides a structure in the catholyte chamber which enables force closure through the entire cell area. Thereby, the GDE is pressed onto Rake1 and the electric current is distributed in the metallic flowfield rather than in the carbon based GDE

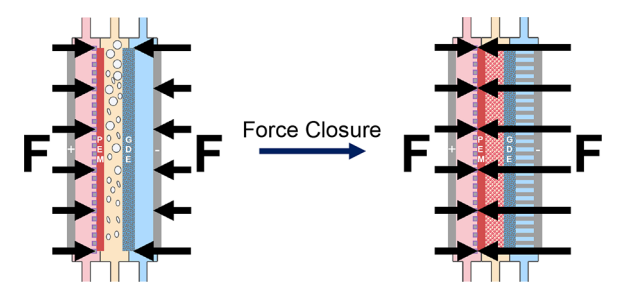


Figure 6. Illustration of the force closure through the cell. Noncomplete force closure for a cell without the spacer and open frame current collector (left) and complete force closure through cell with spacer and flowfield (right).

(Figure 4c). This reduces the electrical ohmic losses and hence U_{Cell} for the cell with the spacer compared to the cell without the spacer.

Furthermore, the measured U_{Cell} determined with the spacer shows significantly reduced noise compared to the ones determined without the spacer. For a better illustration of this effect, U_{Cell} is shown in Figure 7 over the full time for the experiments with Meander. The results of the experiment without the spacer are depicted for different λ in Figure 7(a) and with the spacer in Figure 7(b). Without the spacer, the cell operated at an average $U_{\text{Cell}} \leq 3.8 \text{ V}$ for $\lambda = 4.5$, with the implemented spacer an average value of $U_{\text{Cell}} = 3.95 \text{ V}$ was determined. Comparing U_{Cell} at lower λ , similar differences between the two experiments can be observed.

Figure 7(a) shows extreme noise (e.g., standard deviation = $0.08 \text{ V} (\lambda = 4.5)$ in the voltage measurements, which indicates voltage instabilities caused by the bubble formation in the catholyte chamber. Figure 7(b) shows in contrast a more stable (e.g., standard-deviation = 0.01 V (λ = 4.5)) but higher cell voltage. To describe the effect of the spacer on U_{Cell} , the current flow is illustrated in Figure 8(a) for a cell containing Chamber1 without a spacer and for a cell containing a flowfield and the spacer. Without the spacer, the current flow is forced to evade around the formed bubbles in the catholyte chamber and is afterward led along the GDE to Chamber1. These deflections of the current flow lead to a local increase of the current density and to the voltage instabilities observed in Figure 7(a). As illustrated in Figure 8(b), the deflections of the current flow can be avoided by implementing the ionically conductive spacer, which bridges the bubbles and provides a

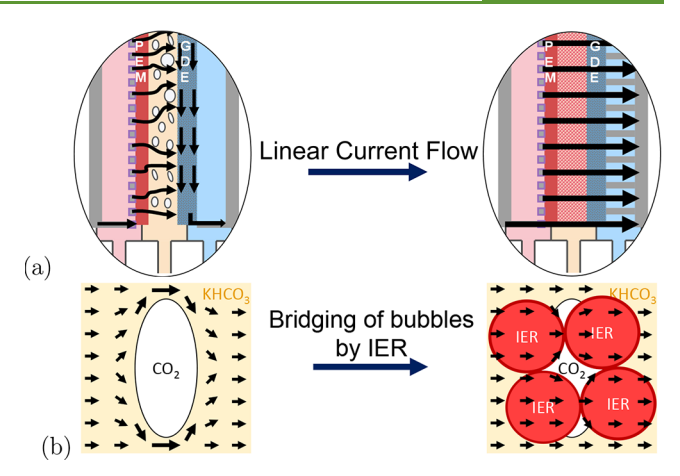


Figure 8. (a) Illustration of the current flow through the cell. ((a)-left) Nonlinear current flow for cell with open frame current collector and without the spacer, ((a)-right) linear current flow for cell with spacer and flowfield. (b) Illustration of current flow through part of the catholyte chamber, ((b)-left) current flow in chamber without a spacer evades around a CO_2 gas bubble, ((b)-right) ion exchange resin (IER) bridges the CO_2 gas bubble and enables a more linear current flow.

linear current flow through the catholyte chamber. $U_{\rm Cell}$ is therefore dependent on the conductivity of the IER, which was determined in this work to be lower in combination with the 1 M KHCO₃ solution, than the conductivity of the pure 1 M KHCO₃ solution. This accompanies the observation of the higher $U_{\rm Cell}$ determined with the spacer compared to the experiment without the spacer. Furthermore, the linear current flow is completed by the flowfield implementation, which provides a larger GDE-current collector contact area and prevents thereby the deflection of the current flow along the GDE.

The results of the experiments performed with pure CO_2 supply and different λ are illustrated in Figure 9. For Chamber1, Meander, Rake1, and Rake2, FE(CO) remained over 90% for $\lambda \geq 2$ and decreases to 40% for $\lambda = 0.5$. While Meander and Chamber1 decline more rapidly, reaching only a FE(CO) of 67% for $\lambda = 1$, for Rake1 and Rake2 a FE(CO) = 79% could be determined. The most rapid decrease of FE(CO) can be observed for Chamber2, decreasing from under 90% for $\lambda = 2$ to 40% for $\lambda = 0.5$. The results show an

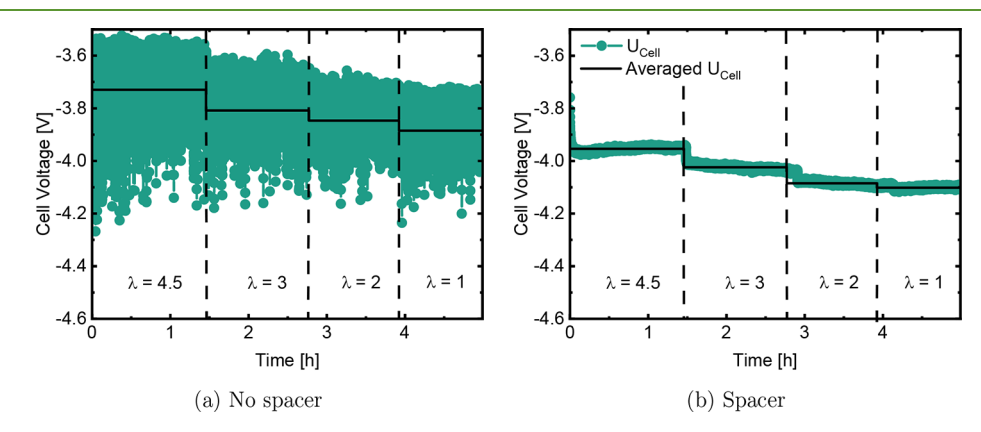


Figure 7. Voltage measurements and averaged U_{Cell} over time for experiment with Meander for different λ at 100 mA/cm². (a) Voltage measurement on cell without the spacer, (b) voltage measurement with ionically conductive spacer show reduction of bubble induced noise in measurement of cell voltage.

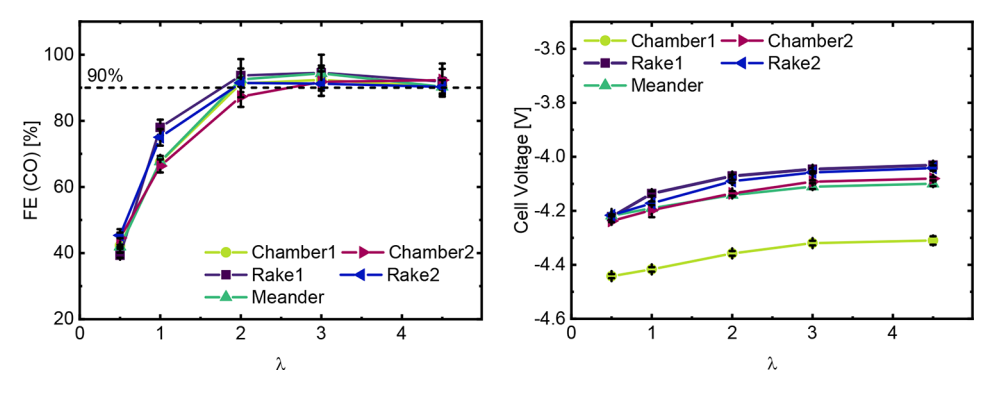


Figure 9. FE(CO) (left) and U_{Cell} (right) over λ for experiments with pure CO₂ feed gas for experiments with Chamber1, Chamber2, Rake1, Rake2, and Meander in cell with spacer at 100 mA/cm².

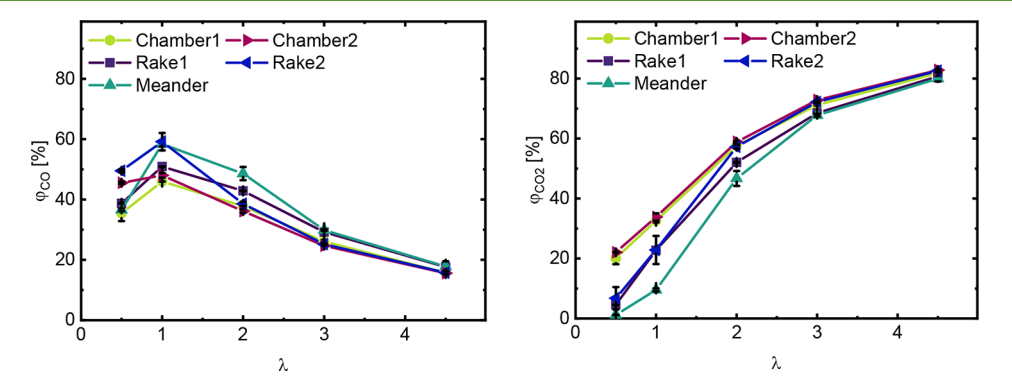


Figure 10. Concentration of CO (φ_{CO}) (left) and concentration of CO₂ (φ_{CO_2}) (right) in the product gas over λ for experiments with Chamber1, Chamber2, Rake1, Rake2, and Meander in cell with spacer operating with pure CO₂ feed gas at 100 mA/cm².

increase of $U_{\rm Cell}$ for decreasing λ for every experiment. Similar $U_{\rm Cell}$ were determined for Rake1 and Rake2, increasing from $U_{\rm Cell}=4.01~{\rm V}$ for $\lambda=4.5$ to $U_{\rm Cell}=4.2~{\rm V}$ for $\lambda=0.5$. For $\lambda=0.5$ the same $U_{\rm Cell}$ was determined for Meander and Chamber2, but in both cases, $U_{\rm Cell}$ increased from $U_{\rm Cell}=4.1~{\rm V}$ for $\lambda=4.5$. The highest $U_{\rm Cell}$ were measured in experiments with Chamber1, increasing from $U_{\rm Cell}=4.3~{\rm V}$ at $\lambda=4.5$ to $U_{\rm Cell}=4.45~{\rm V}$ at $\lambda=0.5$.

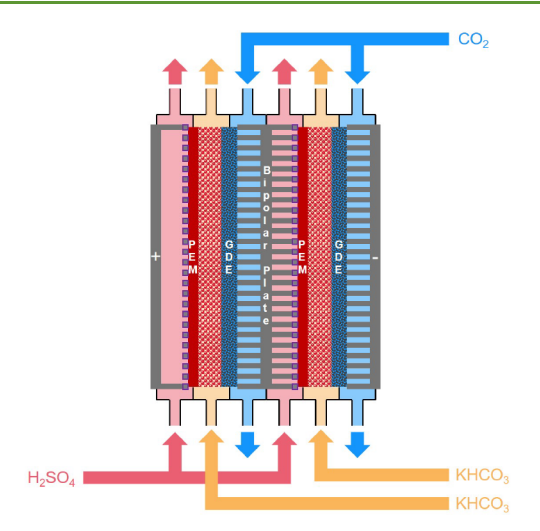
The results in Figure 9 show the positive effect of the optimized feed gas distribution over the GDE, performed by Rake1 and Rake2, on FE(CO) and U_{Cell} for low CO₂ supply (λ = 1). The effect becomes apparent in the comparison of the results obtained with Rake1 and Rake2 to the results obtained with Chamber1. With Chamber1 the maximum GDE-gas contact area is provided, with Rake1 and Rake2 however, a higher FE(CO) is determined for λ = 1. Possible mass transport limitations, appearing with Chamber1, cause the formation concentration gradients in the gas chamber not only along the GDE but also perpendicular to the GDE. Other than with Rake1 and Rake2 not all of the CO₂ which enters the Chamber1 gas chamber is transported to the electrocatalyst surface and can be potentially converted to CO.

For the same experiments, the determined concentrations φ_{CO} and φ_{CO_2} in the product gas are illustrated over λ in Figure 10. In all experiments a $\varphi_{\text{CO}} = 20\%$ for $\lambda = 4.5$ was determined, increasing with decreasing λ . At $\lambda = 1$ the highest φ_{CO} were measured for every experiment, with Rake2 and Meander values of $\varphi_{\text{CO}} \geq 60\%$ being obtained. A further reduction of λ to 0.5 leads to a decrease of φ_{CO} with a maximum value of $\varphi_{\text{CO}} = 50\%$ obtained with Rake2. A decrease of φ_{CO} with

decreasing λ can be observed for all experiments. In all experiments, highest values were measured with $\phi_{\text{CO}_2} \geq 80\%$ for $\lambda = 4.5$. The fastest decrease of ϕ_{CO_2} was observed with Meander, decreasing under 10% for $\lambda = 1$ and under 5% for $\lambda = 0.5$. For Rake1 and Rake2 similar ϕ_{CO_2} values were determined, decreasing to 20% for $\lambda = 1$ and under 10% for $\lambda = 0.5$. With Chamber1 and Chamber2, the higher values of ϕ_{CO_2} were determined, decreasing to 30% for $\lambda = 1$ and to 20% for $\lambda = 0.5$.

 $\phi_{\rm CO}$ increases and $\phi_{\rm CO_2}$ decreases with decreasing λ due to the reduction of the total feed gas volume flow and the high conversion rates. With $\phi_{\rm CO_2}$ decreasing under 10% in experiments with Rake1, Rake2, and Meander one can derive an increase of $\rm CO_2$ consumption compared to experiments with Chamber1 and Chamber2. In the case of Rake1 and Rake2 the increased consumption is accompanied by the higher FE(CO) determined in the experiments. Furthermore, Rake1, Rake2, and Meander can overcome the aforementioned mass transport limitations and can therefore not only increase FE(CO), but also increase the transport of $\rm CO_2$ into the catholyte.

The modifications on the cell design increased the cell performance under reduced CO₂ supply and enabled an ionic and electric contact through the entire active cell area. Aside of the enhanced process parameters, the combination of the modifications formed a cell architecture with mechanically stable components and an even force distribution, ensuring mechanical integrity for the single cell and for a possible stack.



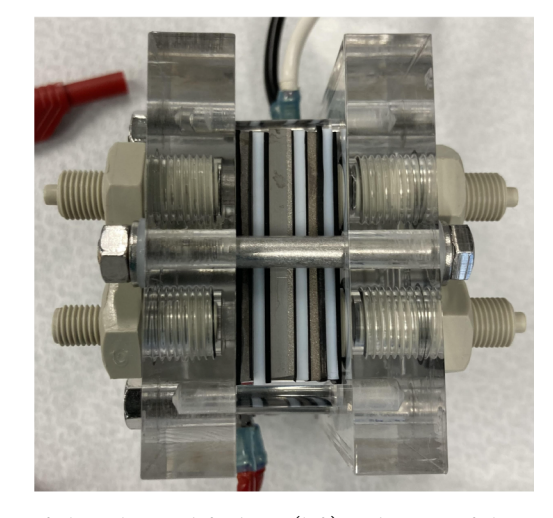


Figure 11. Illustration of the two-cell short-stack including the flowsheet of electrolyte and feed gas (left) and image of the top view of the assembled stack (right). The two cells are connected via a bipolar plate, which provides a gas path architecture similar to Rake1 to the cathode of the first cell (left) and a meander for the anolyte to the second cell (right). The catholyte chambers were filled with the IER beads.

To investigate the cell's performance in a stack, two cells were connected via a bipolar plate to a two-cell short-stack (Figure 11). The used titanium (grade 1) bipolar plate connected the cathode of the first cell to the anode of the second cell and provided a gas path architecture similar to Rake1 to the cathode and a meander electrolyte path similar to Meander to the anode. The global cathode was assembled with Rake1 and the global anode was assembled similar to the previous experiments and the catholyte chambers were filled with the IER beads. The catholyte was introduced to the cell using two different pumps, each of them fed only one catholyte chamber with a volume flow of 50 mL/min. The CO₂ feed gas was supplied parallel to both cathodes sharing the same entrance and exit of the stack. The analyte chambers were supplied parallel with anolyte over a shared entrance and exit with 100 mL/min. A detailed flowsheet for the stack operation mode and the manifolding of the flow media can be found in the Supporting Information. Experiments were conducted at a constant current of 1 A (100 mA/cm²) and a $\lambda = 6.5$ to ensure a sufficient supply of CO₂ to both cathodes. The product gases from both gas chambers and both catholytes were analyzed via the gas chromatograph and FE(CO) was determined. The voltage was measured between the anode of the first cell (Figure 11 left) and the cathode of the second cell (Figure 11 right).

In Figure 12 the obtained FE(CO) (left *y*-axis) and U_{Cell} (right *y*-axis) are depicted over time. Additionally U_{Cell} of two single cells is illustrated in the figure at 7.8 V (2 × 3.9 V). The stack was operating for over 150 min at a minimum cell voltage of $U_{\text{Cell}} \leq 7.8$ V. The determined FE(CO) increased over time to maximum values of $\geq 70\%$ after 100 minutes.

Based on the results obtained from experiments with the stack and in comparison to the performance of the individual single cells, a stackability of the designed flowcell can be deducted. By implementation of the mechanically stable flowfields and spacer, force closure through the individual cells and hence through the stack could be provided. Thereby, an electric and ionic contact is provided through the active stack area resulting in a stack voltage similar to the cell voltage of two individual cells operating with Rake1. However, the stack assembly requires optimization regarding the manifolding of the media flows. For instance, the separation of the CO₂

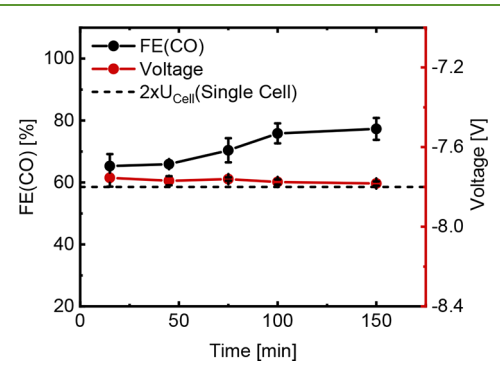


Figure 12. FE(CO) (left y-axis) and U_{Cell} (right y-axis) over time for experiment with stack at 100 mA/cm² and λ = 6.5 and U_{Cell} of two single cells at 7.8 V (2 × 3.9 V).

supply into two individual feed gases could regain control over the pressure and volume flows in the gas chambers. Due to the limitation of entrances for the media in the flowcell, this separation was not possible, and a sufficient and equal supply of CO_2 to the cathodes could not be ensured. The subsequent uneven distribution caused FE(CO) to be lower with the stack, than with the single cell (Figure 9), despite operating with a higher λ in the experiment with the stack.

CONCLUSION

This work demonstrates the potential of improving the flowcells performance by optimizing the feed gas distribution over the GDE area and the media flow in the catholyte chamber. It was demonstrated that the increase of the GDE-gas contact area leads to an increase of the conversion rates of $\rm CO_2$ -to-CO under diluted and reduced $\rm CO_2$ supply, but it conditions a trade-off with the GDE-current collector contact area which, when increased, leads to a reduction of the cell voltage. An optimization toward a more efficient version of this trade-off was demonstrated by an optimized distribution of the feed gas over the GDE with an open gas path architecture, which forces the feed gas through the GDE and creates thereby large GDE-gas and GDE-current collector contact areas simultaneously. The optimized feed gas distribution additionally led to an increase of FE(CO) in experiments with reduced

feed gas volume flow, where mass transport limitations are most severe. These characteristics influence the CO₂ consumption of CO₂-to-CO electrolyzers by generating high selectivity under reduced CO2 supply and by keeping this high selectivity even under diluted supply. Regarding the modification of the catholyte chamber, the implementation of an ionically conductive spacer reduced the nonconductive areas which appeared in the form of gas bubbles. A more linear current flow through the catholyte chamber was created resulting in a more stable process. Furthermore, the combined modifications provided the cell with the necessary mechanical stability to assemble a two-cell short-stack. While improvements on the manifolding of the feed gas need to be executed to raise the performance of the stack to the performance of the single cell, experiments with the stack demonstrated that the designed cell fulfilled the prerequisites for a scaleup.

ASSOCIATED CONTENT

Solution Supporting Information

The Supporting Information is available free of charge at https://pubs.acs.org/doi/10.1021/acssuschemeng.2c05539.

Description of experimental process design for stack and single cell, description of treatment of ions exchange resign and list of materials. Supplementary measurements of temperature, differential pressure and pH-value in the catholyte chamber (PDF)

AUTHOR INFORMATION

Corresponding Author

Maximilian Quentmeier — Institute of Physical Chemistry, RWTH Aachen University, 52074 Aachen, Germany; Institute of Energy and Climate Research, Forschungszentrum Jülich GmbH, 52425 Jülich, Germany; orcid.org/0000-0003-0495-9414; Email: m.quentmeier@fz-juelich.de

Authors

Bernhard Schmid – Institute of Energy and Climate Research, Forschungszentrum Jülich GmbH, 52425 Jülich, Germany Hermann Tempel – Institute of Energy and Climate Research, Forschungszentrum Jülich GmbH, 52425 Jülich, Germany; orcid.org/0000-0002-9794-6403

Hans Kungl – Institute of Energy and Climate Research, Forschungszentrum Jülich GmbH, 52425 Jülich, Germany Rüdiger-A. Eichel – Institute of Physical Chemistry, RWTH Aachen University, 52074 Aachen, Germany; Institute of Energy and Climate Research, Forschungszentrum Jülich GmbH, 52425 Jülich, Germany; orcid.org/0000-0002-0013-6325

Complete contact information is available at: https://pubs.acs.org/10.1021/acssuschemeng.2c05539

Notes

The authors declare no competing financial interest.

ACKNOWLEDGMENTS

The authors kindly acknowledge funding by the Federal Ministry of Education and Research (BMBF), Project: iNEW2.0 'Inkubator Nachhaltige Elektrochemie' Funding code: 03SF0627A. The authors thank Sebastian B. C. Lehmann for the contributions in graphical designs.

REFERENCES

- (1) Delacourt, C.; Ridgway, P. L.; Kerr, J. B.; Newman, J. Design of an Electrochemical Cell Making Syngas (CO+H₂) from CO₂ and H₂O Reduction at Room Temperature. *J. Electrochem. Soc.* **2008**, *155*, R42
- (2) Endrődi, B.; Bencsik, G.; Darvas, F.; Jones, R.; Rajeshwar, K.; Janáky, C. Continuous-flow electroreduction of carbon dioxide. *Prog. Energy Combust. Sci.* **2017**, *62*, 133–154.
- (3) Jouny, M.; Luc, W.; Jiao, F. General Techno-Economic Analysis of CO₂ Electrolysis Systems. *Ind. Eng. Chem. Res.* **2018**, *57*, 2165–2177.
- (4) Reinisch, D.; Schmid, B.; Martić, N.; Krause, R.; Landes, H.; Hanebuth, M.; Mayrhofer, K. J.; Schmid, G. Various CO₂-to-CO Electrolyzer Cell and Operation Mode Designs to avoid CO₂-Crossover from Cathode to Anode. *Zeitschrift für Physikalische Chemie* **2020**, 234, 1115.
- (5) Masel, R. I.; Liu, Z.; Yang, H.; Kaczur, J. J.; Carrillo, D.; Ren, S.; Salvatore, D.; Berlinguette, C. P. An industrial perspective on catalysts for low-temperature CO_2 electrolysis. *Nat. Nanotechnol.* **2021**, *16*, 118–128.
- (6) Haas, T.; Krause, R.; Weber, R.; Demler, M.; Schmid, G. Technical photosynthesis involving CO₂ electrolysis and fermentation. *Nature Catalysis* **2018**, *1*, 32–39.
- (7) Salvatore, D. A.; Weekes, D. M.; He, J.; Dettelbach, K. E.; Li, Y. C.; Mallouk, T. E.; Berlinguette, C. P. Electrolysis of Gaseous CO_2 to CO in a Flow Cell with a Bipolar Membrane. *ACS Energy Letters* **2018**, 3, 149–154.
- (8) Liu, Z.; Yang, H.; Kutz, R.; Masel, R. I. CO₂ Electrolysis to CO and O₂ at High Selectivity, Stability and Efficiency Using Sustainion Membranes: Journal of The Electrochemical Society, 165(15), J3371-J3377. *J. Electrochem. Soc.* **2018**, *165*, J3371–J3377.
- (9) Küngas, R. Review—Electrochemical CO 2 Reduction for CO Production: Comparison of Low- and High-Temperature Electrolysis Technologies. *J. Electrochem. Soc.* **2020**, *167*, 044508.
- (10) Higgins, D.; Hahn, C.; Xiang, C.; Jaramillo, T. F.; Weber, A. Z. Gas-Diffusion Electrodes for Carbon Dioxide Reduction: A New Paradigm. *ACS Energy Letters* **2019**, *4*, 317–324.
- (11) Weekes, D. M.; Salvatore, D. A.; Reyes, A.; Huang, A.; Berlinguette, C. P. Electrolytic CO₂ Reduction in a Flow Cell. Accounts of chemical research **2018**, 51, 910–918.
- (12) Kutz, R. B.; Chen, Q.; Yang, H.; Sajjad, S. D.; Liu, Z.; Masel, I. R. Sustainion Imidazolium-Functionalized Polymers for Carbon Dioxide Electrolysis. *Energy Technology* **2017**, *5*, 929–936.
- (13) Larrazábal, G. O.; Strøm-Hansen, P.; Heli, J. P.; Zeiter, K.; Therkildsen, K. T.; Chorkendorff, I.; Seger, B. Analysis of Mass Flows and Membrane Cross-over in CO₂ Reduction at High Current Densities in an MEA-Type Electrolyzer. *ACS Appl. Mater. Interfaces* **2019**, *11*, 41281–41288.
- (14) Liang, S.; Altaf, N.; Huang, L.; Gao, Y.; Wang, Q. Electrolytic cell design for electrochemical CO_2 reduction. *J. CO2 Utilization* **2020**, 35, 90–105.
- (15) Lee, C.; Zhao, B.; Lee, J. K.; Fahy, K. F.; Krause, K.; Bazylak, A. Bubble Formation in the Electrolyte Triggers Voltage Instability in CO_2 Electrolyzers. *iScience* **2020**, 23, 101094.
- (16) Rabinowitz, J. A.; Kanan, M. W. The future of low-temperature carbon dioxide electrolysis depends on solving one basic problem. *Nat. Commun.* **2020**, *11*, 5231.
- (17) Subramanian, S.; Middelkoop, J.; Burdyny, T. Spatial reactant distribution in CO₂ electrolysis: balancing CO₂ utilization and faradaic efficiency. Sustainable Energy & Fuels **2021**, 5, 6040–6048.
- (18) Li, Y. C.; Zhou, D.; Yan, Z.; Gonçalves, R. H.; Salvatore, D. A.; Berlinguette, C. P.; Mallouk, T. E. Electrolysis of CO₂ to Syngas in Bipolar Membrane-Based Electrochemical Cells. *ACS Energy Letters* **2016**, *1*, 1149–1153.
- (19) Krause, R.; Reinisch, D.; Reller, C.; Eckert, H.; Hartmann, D.; Taroata, D.; Wiesner-Fleischer, K.; Bulan, A.; Lueken, A.; Schmid, G. Industrial Application Aspects of the Electrochemical Reduction of CO₂ to CO in Aqueous Electrolyte. *Chemie Ingenieur Technik* **2020**, 92, 53–61.

- (20) Endrődi, B.; Kecsenovity, E.; Samu, A.; Darvas, F.; Jones, R. V.; Török, V.; Danyi, A.; Janáky, C. Multilayer Electrolyzer Stack Converts Carbon Dioxide to Gas Products at High Pressure with High Efficiency. *ACS Energy Letters* **2019**, *4*, 1770–1777.
- (21) Millet, P.; Ngameni, R.; Grigoriev, S. A.; Mbemba, N.; Brisset, F.; Ranjbari, A.; Etiévant, C. PEM water electrolyzers: From electrocatalysis to stack development. *Int. J. Hydrogen Energy* **2010**, 35, 5043–5052.
- (22) Marx, N.; Boulon, L.; Gustin, F.; Hissel, D.; Agbossou, K. A review of multi-stack and modular fuel cell systems: Interests, application areas and on-going research activities. *Int. J. Hydrogen Energy* **2014**, *39*, 12101–12111.
- (23) Napporn, T. W.; Karpenko-Jereb, L.; Pichler, B.; Hacker, V. In Fuel cells and hydrogen; Hacker, V., Mitsushima, S., Eds.; Elsevier: Amsterdam and Oxford and Cambridge, MA, 2018; pp 63–89.
- (24) Blank, F. In *Polymer Electrolyte Fuel Cell Durability*; Büchi, F. N., Inaba, M., Schmidt, T. J., Eds.; Springer New York: New York, NY, 2009; pp 419–430.
- (25) Burney, H. S.; White, R. E. Predicting Shunt Currents in Stacks of Bipolar Plate Cells with Conducting Manifolds. *J. Electrochem. Soc.* **1988**, *135*, 1609–1612.
- (26) Leonard, M. E.; Clarke, L. E.; Forner-Cuenca, A.; Brown, S. M.; Brushett, F. R. Investigating Electrode Flooding in a Flowing Electrolyte, Gas-Fed Carbon Dioxide Electrolyzer. *ChemSusChem* **2020**, *13*, 400–411.
- (27) Han, J.-H.; Hwang, K.-s.; Jeong, H.; Byeon, S.-Y.; Nam, J.-Y.; Kim, C.-S.; Kim, H.; Yang, S.; Choi, J. Y.; Jeong, N. Electrode system for large-scale reverse electrodialysis: water electrolysis, bubble resistance, and inorganic scaling. *J. Appl. Electrochem.* **2019**, 49, 517–528.
- (28) Zhang, B.; Gao, H.; Chen, Y. Enhanced Ionic Conductivity and Power Generation Using Ion-Exchange Resin Beads in a Reverse-Electrodialysis Stack. *Environ. Sci. Technol.* **2015**, 49, 14717–14724.
- (29) Dejean, E.; Laktionov, E.; Sandeaux, J.; Sandeaux, R.; Pourcelly, G.; Gavach, C. Electrodeionization with ion-exchange textile for the production of high resistivity water: Influence of the nature of the textile. *Desalination* 1997, 114, 165–173.
- (30) Golubenko, D. V.; Křivčík, J.; Yaroslavtsev, A. B. Evaluating the effectiveness of ion exchangers for the electrodeionization process. *Petroleum Chemistry* **2015**, *55*, 769–775.
- (31) Korngold, E. Electrodialysis processes using ion exchange resins between membranes. *Desalination* **1975**, *16*, 225–233.
- (32) Yang, H.; Kaczur, J. J.; Sajjad, S. D.; Masel, R. I. Electrochemical conversion of CO₂ to formic acid utilizing Sustainion membranes. *J CO2 Utilization* **2017**, *20*, 208–217.

☐ Recommended by ACS

Enhancing Electrocatalytic Hydrodechlorination through Interfacial Microenvironment Modulation

Zhimin Fan, Rui Liu, et al.

JANUARY 08, 2023

ENVIRONMENTAL SCIENCE & TECHNOLOGY

READ 🗹

Fabrication of Flower-like Rhodium-Doped β -Ni(OH) $_2$ as an Efficient Electrocatalyst for Methanol Oxidation Reaction in Alkaline Media

Yafeng Wang, Yanqing Yang, et al.

DECEMBER 22, 2022

LANGMUIR

READ 🗹

Understanding the Roles of Hydroxide in CO₂ Electroreduction on a Cu Electrode for Achieving Variable Selectivity

Mingxu Sun, Miho Yamauchi, et al

NOVEMBER 22, 2022

ACS CATALYSIS

READ **C**

 Fe_3O_4 -Functionalized κ -Carrageenan/Melanin Hybrid Aerogel-Supported Form-Stable Phase-Change Composites with Excellent Solar/Magnetic-Thermal Conversion Effic...

Linzhao Jin, Zongliang Du, et al.

JANUARY 05, 2023

ACS SUSTAINABLE CHEMISTRY & ENGINEERING

READ 🗹

Get More Suggestions >